





Cite this: *RSC Adv.*, 2019, 9, 13820

# Rosette-like MoS<sub>2</sub> nanoflowers as highly active and stable electrodes for hydrogen evolution reactions and supercapacitors†

Xuexia Liu,<sup>a</sup> Limin Liu,<sup>a</sup> Ying Wu,<sup>a</sup> Yinfeng Wang,<sup>a</sup> Jinhu Yang<sup>b</sup> <sup>b</sup> and Zhijun Wang<sup>a\*</sup> 

MoS<sub>2</sub> is regarded as one of the cost-effective materials for many important applications. In this work, we report a simple one-step hydrothermal method for the directed synthesis of a rosette-like MoS<sub>2</sub> nanoflower modified electrode without using adhesion agents. Interestingly, owing to the hierarchical structures, the as-prepared MoS<sub>2</sub>-based electrode exhibits significantly enhanced performance for both the hydrogen evolution reaction in acidic environments and supercapacitors. When used in the hydrogen evolution reaction, the electrode shows a low overpotential of ~0.25 V at 10 mA cm<sup>-2</sup>, a Tafel slope of ~71.2 mV per decade, and long-term durability over 20 h of hydrogen evolution reaction operation at 10 mV cm<sup>-2</sup>. In addition, as a supercapacitor electrode, it exhibits a good capacity of 137 mF cm<sup>-2</sup> at a current density of 10 mA cm<sup>-2</sup> and excellent stability in 1 M H<sub>2</sub>SO<sub>4</sub> at a scan rate of 50 mV s<sup>-1</sup>. The outstanding performances of the as-prepared materials may be ascribed to the unique 3D architectures of the rosette-like MoS<sub>2</sub> nanoflowers. This work could provide a strategy to explore low-cost and highly efficient electrocatalysts with desired nanostructures for the hydrogen evolution reaction and supercapacitors applications.

Received 13th February 2019  
 Accepted 28th April 2019

DOI: 10.1039/c9ra01111k

[rsc.li/rsc-advances](http://rsc.li/rsc-advances)

## 1. Introduction

Nowadays, owing to concerns regarding the environment and the gradual depletion of nonrenewable resources, for example coal, oil and natural gas, developing sustainable and clean energy sources has become an effective way for human beings to deal with the energy crisis.<sup>1–3</sup> Hydrogen, as a clean and sustainable energy carrier,<sup>4,5</sup> is an economic fuel in electric devices.<sup>6</sup> The low cost, high efficiency and renewable electric devices, such as supercapacitors,<sup>7</sup> lithium ion batteries (LIBs)<sup>8,9</sup> and fuel cells, have become important alternative electrochemical devices to fossil fuels. The hydrogen evolution reaction (HER) is an effective and convenient process to produce molecular hydrogen from water. To our knowledge, noble Pt and Pt-based materials are regarded as the most effective and catalytically stable electrocatalysts for HER,<sup>10</sup> particularly in acid solution.<sup>11,12</sup> However, global-scale application is challenged by their high cost and limited supply.<sup>13–15</sup> Recently, tremendous effort has focused on investigating the possibility of earth abundant elements catalytic performances HER

electrocatalysts for large-scale hydrogen production,<sup>16</sup> such as sulfide,<sup>17,18</sup> nitride,<sup>19</sup> boride,<sup>20</sup> and phosphide.<sup>21</sup> Among them, molybdenum disulfide (MoS<sub>2</sub>) based on molybdenum element possesses attracting electrochemical properties, for instance, defective nanosheets,<sup>22</sup> porous films,<sup>23</sup> double-gyroid structures,<sup>24</sup> nanowires<sup>25</sup> and amorphous films.<sup>26</sup> Especially, the MoS<sub>2</sub> of single-layer, few-layer or re-stacked layer forms held together by van der Waals forces has been widely used as electrocatalyst for HER.<sup>27–30</sup> It is well known that two-dimensional (2D) layered MoS<sub>2</sub> possesses unique electrical and chemical properties due to their large exposure of active sites<sup>31</sup> caused by the coordinatively unsaturated sulfur atoms at the edge sites.<sup>32</sup> Meanwhile, MoS<sub>2</sub> has also been considered as an ideal material for supercapacitors, which is due to that the ultrathin layer forms structure has large surface area for double-layer charge storage and the central Mo atoms has great potential for pseudocapacitance from the H<sup>+</sup> intercalation into the stacked layers.<sup>33</sup> And the interlayer spacing (002) is crucial for the insertion of foreign atoms<sup>34</sup> and electrolyte diffusion. Nevertheless, the synthesis of large layer forms MoS<sub>2</sub> nanostructure is still a challenge because of the difficulty of preparation of these species.

Also, the utilization of 2D nanomaterials suffers from inadequate contact with electrolyte and low surface-area-utilization efficiency. In order to resolve this problem, extensive efforts have been devoted to assembling 2D materials into 3D architecture.<sup>35,36</sup> The construction of 3D framework is a best strategy

<sup>a</sup>School of Chemistry and Chemical Engineering, Jinggangshan University, Ji'an, Jiangxi 343009, PR China. E-mail: wangzj1223@163.com

<sup>b</sup>School of Chemical Science and Engineering, Tongji University, Shanghai 200092, PR China

† Electronic supplementary information (ESI) available. See DOI: 10.1039/c9ra01111k



to increase the diffusion of the ions and electrolyte into materials, which is favorable for promoting the electrochemical performance of the materials.

Herein, we report a simple strategy to synthesize an interlayer spacing-enlarged rosette-like MoS<sub>2</sub> nanoflowers for both hydrogen evolution reaction and supercapacitive energy storage. In the synthesis, (NH<sub>4</sub>)<sub>6</sub>Mo<sub>7</sub>O<sub>24</sub>·4H<sub>2</sub>O was used as a Mo resource and thiourea was used as a S resource, and the rosette-like MoS<sub>2</sub> nanoflowers modified electrode was prepared by a one-step hydrothermal method. The synthesized novel MoS<sub>2</sub> structure has the advantages as following: (i) simple and environmental friendly preparation route; (ii) 3D interconnected frameworks to facilitate the electrolyte diffusion; (iii) much more electrochemically active sites to deliver excellent catalytic properties in HER; (iv) the active materials grown on Ti foil directly used as electrode for electrochemical performance testing; (v) larger interlayer spacing which is beneficial for ion intercalation into S–Mo–S stacked layer; (vi) more importantly, the as-prepared MoS<sub>2</sub> composites are suitable for both HER and supercapacitors.

## 2. Experimental

### 2.1 Chemicals

(NH<sub>4</sub>)<sub>6</sub>Mo<sub>7</sub>O<sub>24</sub>·4H<sub>2</sub>O (Aladdin, 99%) and thiourea (Aladdin, ≥99%) were of analytical grade and used without further purification.

### 2.2 Synthesis of MoS<sub>2</sub>

Typically, 0.57 mmol (NH<sub>4</sub>)<sub>6</sub>Mo<sub>7</sub>O<sub>24</sub>·4H<sub>2</sub>O and 6 mmol thiourea were dissolved into 36 mL of deionized (DI) water in 40 mL Teflon-lined stainless-steel autoclave. After sonicating 20 min, a titanium sheet (0.2 mm, 1 × 5 cm) which was sonicated in 2 M HCl, ethanol and DI water respectively was immersed into the solution. Then, the autoclave was kept at 180 °C for 12 h. After naturally cooling down, the titanium sheet was washed with a large amount of ethanol and DI water, and dried in a vacuum oven at 70 °C for several hours. For comparison, the MoS<sub>2</sub> was also synthesized at the same conditions with synthesis time of 6 and 20 h.

### 2.3 Characterizations

The crystalline structure of the as-prepared MoS<sub>2</sub> nanoflowers was characterized by power X-ray diffraction (XRD) on a D/max2550VB3+/PC X-ray diffractometer with a Cu Kα radiation source (λ = 0.15418 nm). The general morphologies of samples were analyzed by scanning electron microscopy (SEM, Hitachi S-4800) with an X-ray energy dispersive spectroscopy (EDS) analysis system. Transmission electron microscopy (TEM, FEI TF30) and selected area electron diffraction (SAED) were used to observe the morphological properties of the samples. X-ray photoelectron spectroscopy spectra (XPS, EP13-002) were used to investigate the chemical composition.

## 2.4 Electrochemical measurements

All the electrochemical experiments were conducted using a CHI660C electrochemical workstation (Shanghai Chenhua Instruments Co.) with a standard three-electrode cell. And the rosette-like MoS<sub>2</sub> nanoflowers grown on titanium sheet were directly used as working electrodes and graphite rod was used as counter electrode for both HER performance and supercapacitor testing.

**2.4.1 HER measurements.** The saturated calomel electrode was used as reference electrode and all the tests were performed in a N<sub>2</sub> saturated 0.5 M H<sub>2</sub>SO<sub>4</sub> electrolyte. Linear sweep voltammetry (LSV) was performed at scan rates of 2 mV s<sup>−1</sup> with the potential range of −0.6 V to 0 V. The electrochemical impedance spectroscopy (EIS) were performed at open circuit potentials by using the frequency range of 0.1 to 100 kHz with an AC voltage of 5 mV. The stability of the HER was evaluated by amperometric *I*–*t* measurement at the current density of 10 mA cm<sup>−2</sup> for 20 h. All the potentials were converted to the RHE based on the equation  $E(\text{RHE}) = E(\text{SCE}) + (0.242 + 0.059\text{pH}) \text{ V}$ .

**2.4.2 Supercapacitor measurements.** The reference electrode was Ag/AgCl electrode, and a 1 M H<sub>2</sub>SO<sub>4</sub> was employed as the electrolyte. Cyclic voltammetry (CV) measurements was performed from 10 to 800 mV s<sup>−1</sup> within a potential range between −0.2 and 0.4 V. EIS tests were carried out with frequency ranging from 0.01 Hz to 100 kHz with an ac signal amplitude being set as 5 mV. Galvanostatic discharge/charge (GCD) curves were collected at current densities ranging from 1 to 25 mA cm<sup>−2</sup>. The stability of the supercapacitor was evaluated by repeating the CV measurement at a scan rate of 50 mV s<sup>−1</sup> for 10 000 cycles. In a three-electrode system, the specific capacitance was calculated based on CV and GCD curves by eqn (1) and (2), respectively:

$$C_A = \frac{1}{Sv(\Delta V)} \int I(V) dV \quad (1)$$

where *S* is the geometrical area of each film, *v* is the scan rate, Δ*V* is the working potential window, *I*(*V*) is the response current.

$$C_A = \frac{I\Delta t}{S\Delta V} \quad (2)$$

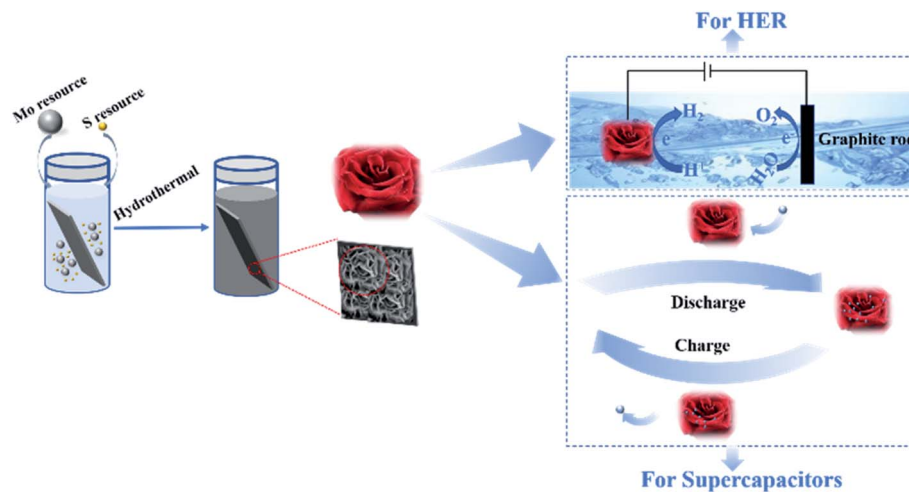
where *I* is the discharge current, Δ*t* is the discharge duration, *S* is geometrical area of each film and Δ*V* is the discharge potential window with deduction of IR drop.

## 3. Results and discussion

### 3.1 Synthesis of rosette-like MoS<sub>2</sub> nanoflowers on Ti foil

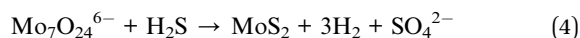
Scheme 1 describes the entire fabrication process of rosette-like MoS<sub>2</sub> nanoflowers architectures. Briefly, ammonium molybdate and thiourea were used as Mo and S resources, respectively. With temperature increasing, H<sub>2</sub>S was generated through the reaction of thiourea and water (reaction (3)). Due to the strong reducibility of the H<sub>2</sub>S, the Mo(vi) atom in Mo<sub>7</sub>O<sub>24</sub><sup>6−</sup> ion could be reduced to Mo(IV) atom, and the Mo(IV) atom reacted with H<sub>2</sub>S to produce MoS<sub>2</sub> according to the reaction (4).<sup>37</sup> As a result, the interlayer S–Mo–S atoms is strongly covalently linked by weak van der Waals forces, and the 3D hierarchical of the





**Scheme 1** Scheme description of the synthetic route of the spacing-enlarged rosette-like MoS<sub>2</sub> nanoflowers that exhibit a remarkable electrochemical performance in both HER and supercapacitors.

rosette-like MoS<sub>2</sub> nanoflowers directly grown on the bottom of the titanium sheet (Fig. S1, ESI†) by the bridge bonds.<sup>38</sup> The whole process was simple, and the hydrothermal reaction is excellent environment-friendly and low-cost.



The morphology and structure of the as-prepared samples is displayed in Fig. 1a, indicating the successful synthesis of rosette-like MoS<sub>2</sub> nanoflowers. In addition, the image (Fig. 1a) clearly reviews that the diameter of the nanoflowers is about 300 nm. The high-magnification SEM images of the

nanoflowers in Fig. 1b and c show that the nanoflowers consists of ultrathin nanosheets with the thickness less than 15 nm. The novel architecture of the MoS<sub>2</sub> is in favor of rapid electron transfer during charge/discharge processes.<sup>39</sup> In addition, the MoS<sub>2</sub> nanomaterials did not exhibit the rosette-like morphology (Fig. S2, ESI†) when the reaction time was 6 h and 20 h. It is speculated that the rosette-like MoS<sub>2</sub> nanoflowers morphology cannot be formed with a relatively shorter reaction time. However, the surface of the nanosheets became disordered with a longer reaction time of 20 h. The uniform distribution of elements Mo and S throughout the whole rosette-like MoS<sub>2</sub> nanoflowers can also be evidenced by elemental mapping images (Fig. S3, ESI†). Additionally, the crystalline structure of rosette-like MoS<sub>2</sub> nanoflowers is confirmed by the X-ray diffraction (XRD) pattern. As shown in Fig. S4,† the diffraction

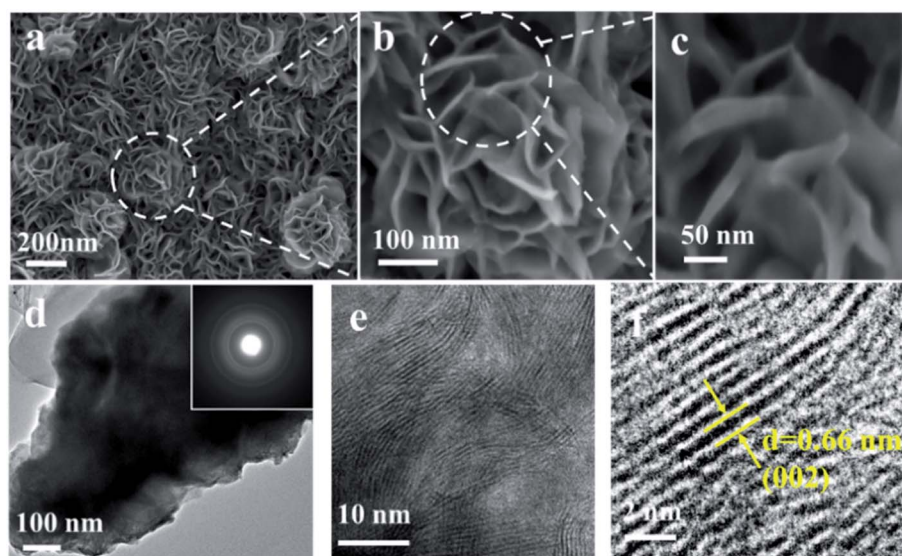


**Fig. 1** (a–c) SEM images of the rosette-like MoS<sub>2</sub> nanoflowers; (d) TEM and (e and f) HRTEM images of a rosette-like MoS<sub>2</sub> nanoflowers. The insets in (d) is the SAED pattern of the as-prepared samples.



peaks at  $2\theta = 10.7^\circ$  is indexed to the (002) peak of the  $\text{MoS}_2$ , which appears a large shift to the left compared with the hexagonal-phase  $\text{MoS}_2$  (JCPDS card no. 37-1492), confirming that the interlayer spacing between the (002) planes are sufficiently expanded. Fig. 1d–f show the TEM and high resolution TEM (HRTEM) of the rosette-like  $\text{MoS}_2$  nanoflowers. The regular lattices in the SAED ring patterns (the inset of Fig. 1d) verify that the hexagonal-structured  $\text{MoS}_2$  is generated.<sup>40,41</sup> Fig. 1e clearly reveals that typical stripe-like nanocrystals of layered  $\text{MoS}_2$  are formed. In addition, the interlayer spacing of the  $\text{MoS}_2$  nanoflowers is sufficiently increasing to 0.66 nm (Fig. 1f) which is larger than the spacing 0.61 nm of bulk  $\text{MoS}_2$ , indicating the low ion diffusion resistance.<sup>42</sup> Therefore, the aforementioned analysis confirms the formation of rosette-like  $\text{MoS}_2$  nanoflowers with interlayer distance can be easily fabricated by the one-step hydrothermal method.

To confirm the chemical composition of the as-prepared rosette-like  $\text{MoS}_2$  nanoflowers, X-ray photoelectron spectroscopy (XPS) was conducted (Fig. 2). The wide scan XPS spectrum (Fig. 2a) revealed five typical peaks corresponding to the binding energies of Mo 3d, Mo 3p, S 2p, C 1s and O 1s orbitals. The signals of the C and O originated from the  $\text{CO}_2$  and  $\text{H}_2\text{O}$  impurities caused by surface adsorption and contamination.<sup>43</sup> High-resolution Mo 3d XPS spectrum in Fig. 2b, the peaks at around 228.6 and 232 eV are corresponding to the  $3d_{5/2}$  and  $3d_{3/2}$  states, respectively. Besides these two peaks, the small peak located at 225.9 eV is indexed as S 2s. Similarly, in Fig. 2c, the peaks at 161.5 and 162.6 eV are assigned to the S  $2p_{3/2}$  and S  $2p_{1/2}$  states, respectively. The binding energies are in excellent agreement with the values for  $\text{MoS}_2$ , confirm the formation of  $\text{MoS}_2$ .<sup>44,45</sup>

### 3.2 Electrochemical characterizations of rosette-like $\text{MoS}_2$ nanoflowers

The electrocatalytic HER activities of the as-prepared rosette-like  $\text{MoS}_2$  nanoflowers catalysts were evaluated in acidic (0.5 M  $\text{H}_2\text{SO}_4$ ) condition with a typical three-electrode configuration. The linear sweep voltammetry (LSV) curves of as-prepared catalysts and bare Ti foil are displayed in Fig. 3a. As expected, the rosette-like  $\text{MoS}_2$  nanoflowers catalyst with a growing time of 12 h exhibits excellent catalytic activity with

a low overpotential of 0.25 V vs. RHE to drive a current density of  $10 \text{ mA cm}^{-2}$ . For comparison, similar measurements on nanomaterials for 6 h and 20 h were also performed. The nanoflowers for 12 h exhibit much larger current density at the same potential than those of nanomaterials for 6 h and 20 h, suggesting that the exceptional HER electrocatalytic activity of the nanoflowers for 12 h. When compare with previous notable works of the  $\text{MoS}_2$  catalyst, the performance of the nanoflowers for 12 h is comparable (Table S1†). The excellent catalytic activity is attributed to the ‘petal effect’ of the rosette-like nanoflowers of the sample for 12 h, which can raise the adhesion of the sample to water.<sup>46,47</sup> Also, the enlarged interlayer spacing of the rosette-like  $\text{MoS}_2$  nanoflowers could accelerate the transmission of the materials in the materials, which is profitable to enhance the HER activity of the sample for 12 h. In order to estimate the reaction kinetics and the rate-determining step for the HER process, the Tafel slope of the samples is plotted using the equation  $\eta = a + b \log(j)$ , where  $a$  is the intercept,  $b$  is the Tafel slope and  $j$  is the current density.<sup>48</sup> Based on the equation, the linear parts of the Tafel plots are shown in Fig. 3b, revealing that the Tafel slopes are about  $\sim 67.5$ , 71.4 and 71.2 mV per decade for the three as-prepared nanomaterials with synthesis time of 6 h, 12 h and 20 h, respectively. The results indicate that the Volmer reaction is taking place and the hydrogen generation reaction follows a fast Volmer–Heyrovsky mechanism.<sup>49,50</sup> Importantly, the low Tafel slope confirms the favorable HER kinetics,<sup>48</sup> which is ascribed to the unique 3D hierarchical architectures that provide more pathways for ion transport.

The Nyquist plots can demonstrate the rate of the ion diffusion during HER, and the shorter the length of the Warburg-type line, the faster of the ion diffusion process from the outside electrolyte into the inner of the catalyst. To gain more insights into the roles of rosette-like structure in promoting the HER activity, the electrochemical impedance spectroscopy was explored. The charge transfer resistance ( $R_{ct}$ ) from the Fig. 3c coupled the contact resistance ( $R_s$ ) from the inset in Fig. 3c demonstrate that rosette-like  $\text{MoS}_2$  nanoflowers exhibits superior HER kinetics due to the enhanced ion transport in the materials. Very importantly, the long-term electrochemical durability is another important criterion to evaluate the catalytic performance of the HER catalyst, and the stability

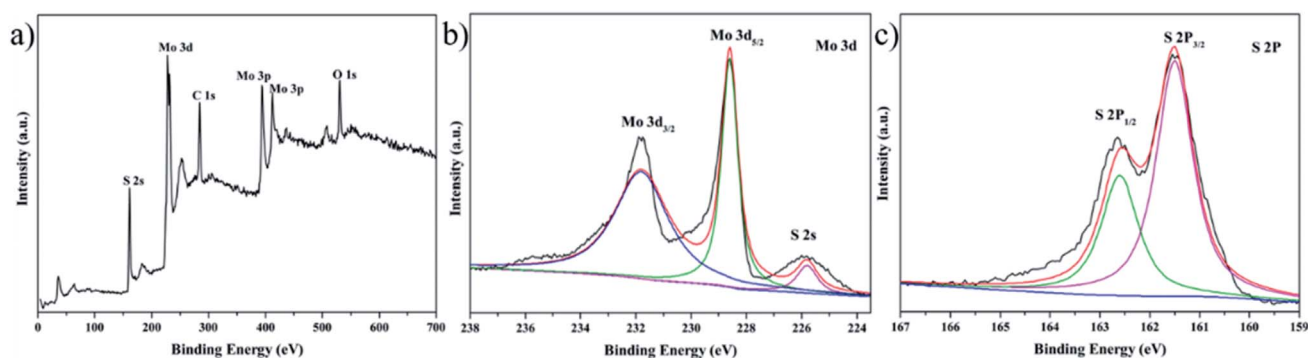


Fig. 2 Structure characterization of the  $\text{MoS}_2$  for 12 h. (a) XPS survey spectrum of the rosette-like  $\text{MoS}_2$  nanoflower; (b) Mo 3d and (c) S 2p.





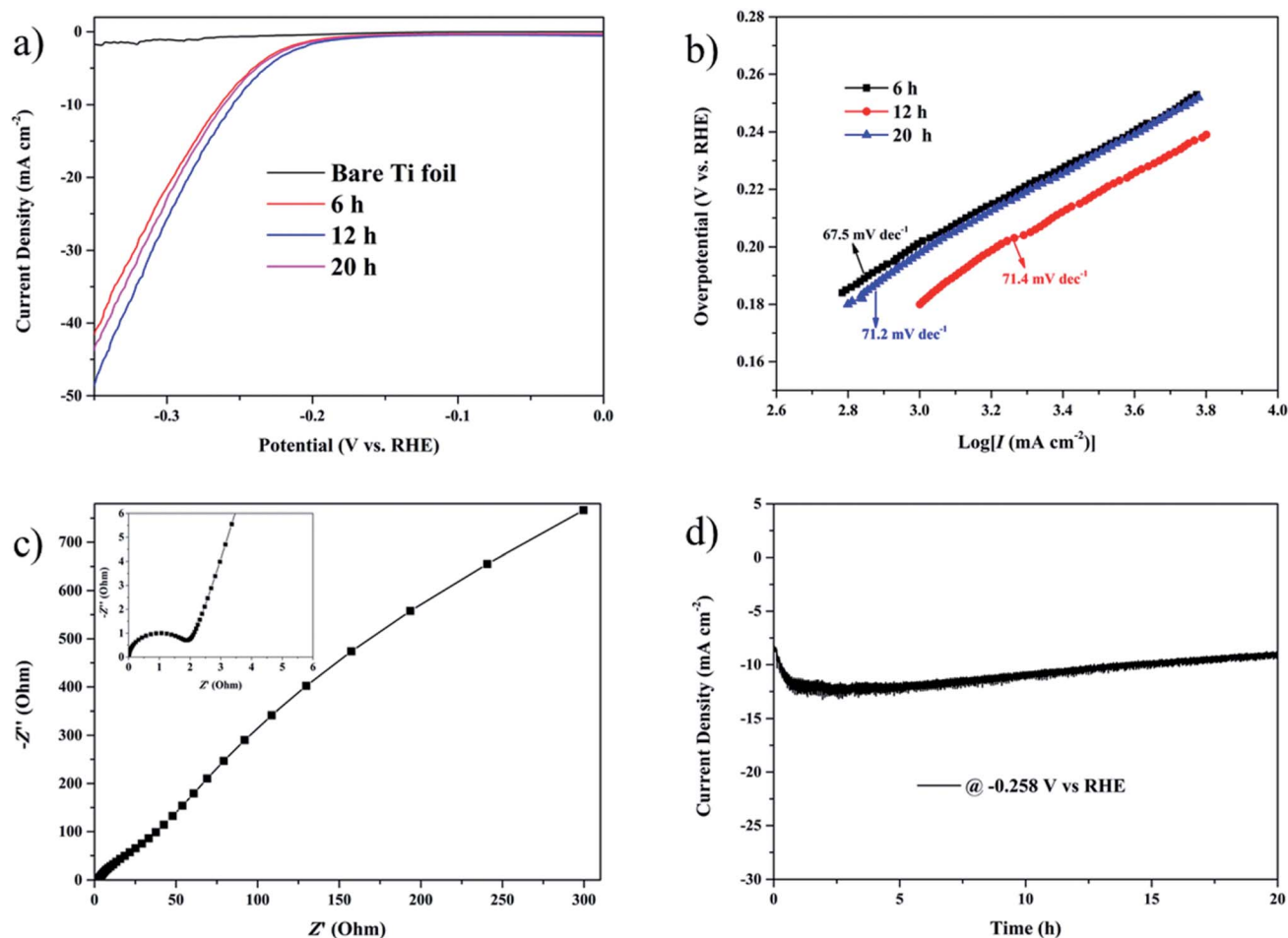


Fig. 3 Electrochemical performance of catalysts for HER in 0.5 M H<sub>2</sub>SO<sub>4</sub>. (a) Linear sweep voltammetry (LSV) curves of bare Ti foil and the rosette-like MoS<sub>2</sub> nanoflowers with different synthesis time; (b) the relevant Tafel curves derived from the polarization curves; (c) Nyquist plots of the catalyst for 12 h at open circuit potentials; (d) amperometric *I*-*t* curves of the catalyst for 12 h over 20 h.

of rosette-like MoS<sub>2</sub> nanoflowers was examined at the current density of 10 mV cm<sup>-2</sup> in acid condition (Movie 1, ESI†). As shown in Fig. 3d, the current density is stabilized after 20 h and only a very slight negative shift is observed in the polarization curve of the sample comparing with the initial polarization curve (Fig. S5, ESI†), indicating its superior durability for HER in acid condition. With regard to both activity and stability, the rosette-like MoS<sub>2</sub> nanoflowers for 12 h represent as an outstanding HER electrocatalyst.

Besides utilization in HER, the as-prepared rosette-like MoS<sub>2</sub> nanoflowers also plays an important role in energy storage. When used as an electrode material in supercapacitors, the electrochemical behavior of the rosette-like MoS<sub>2</sub> nanoflowers is studied in 1.0 M aqueous H<sub>2</sub>SO<sub>4</sub> with a potential interval from -0.2 to 0.4 V in a three-electrode system. Fig. 4a shows the CV curves at different scan rates, ranging from 10 to 800 mV s<sup>-1</sup>. Obviously, all the CV curves display an irregular rectangular shape with a little reduction peak, proving the presence of a double-layer capacitor (EDLC)<sup>51</sup> along with a pseudocapacitive and irreversible faradaic reactions. In addition, the area under the CV curves increases with the increasing of scan rate,<sup>52</sup> and

the estimated area specific capacitance (*C<sub>A</sub>*) values in Fig. 4b based on the CV curves decrease steadily with the increased scan rate, which can be ascribed to the difficulty in ion transport at high scan rates.<sup>53</sup> The *C<sub>A</sub>* value can achieve 71 mF cm<sup>-2</sup> at the scan rate of 50 mV s<sup>-1</sup>, which is larger than the values of the samples for 6 and 20 h based on Fig. S6a.† This indicated that the as-prepared sample for 12 h has superior performance when compared with the samples for other hydrothermal time. Also, the shape of CV curves retains a good rectangular CV shape even at a higher scan rate of 800 mV s<sup>-1</sup>, which indicates a good electrochemical stability and rate performance of the sample. Furthermore, the typical capacitance enhancement at negative potentials indicates the easy charge/discharge of positively charges ions.<sup>54</sup> Also, the galvanostatic charging-discharging (GCD) curves of the rosette-like MoS<sub>2</sub> nanoflowers in Fig. 4c are performed in the potential window from -0.2 to 0.4 V to determine the capacitance dependence on different current density, ranging from 1 to 25 mA cm<sup>-2</sup>. And the quasi-triangular shapes can also indicate the mechanism for the EDLC-pseudocapacitance combined behavior of the supercapacitors. Based on eqn (2), the specific capacitances (*C<sub>A</sub>*) at the



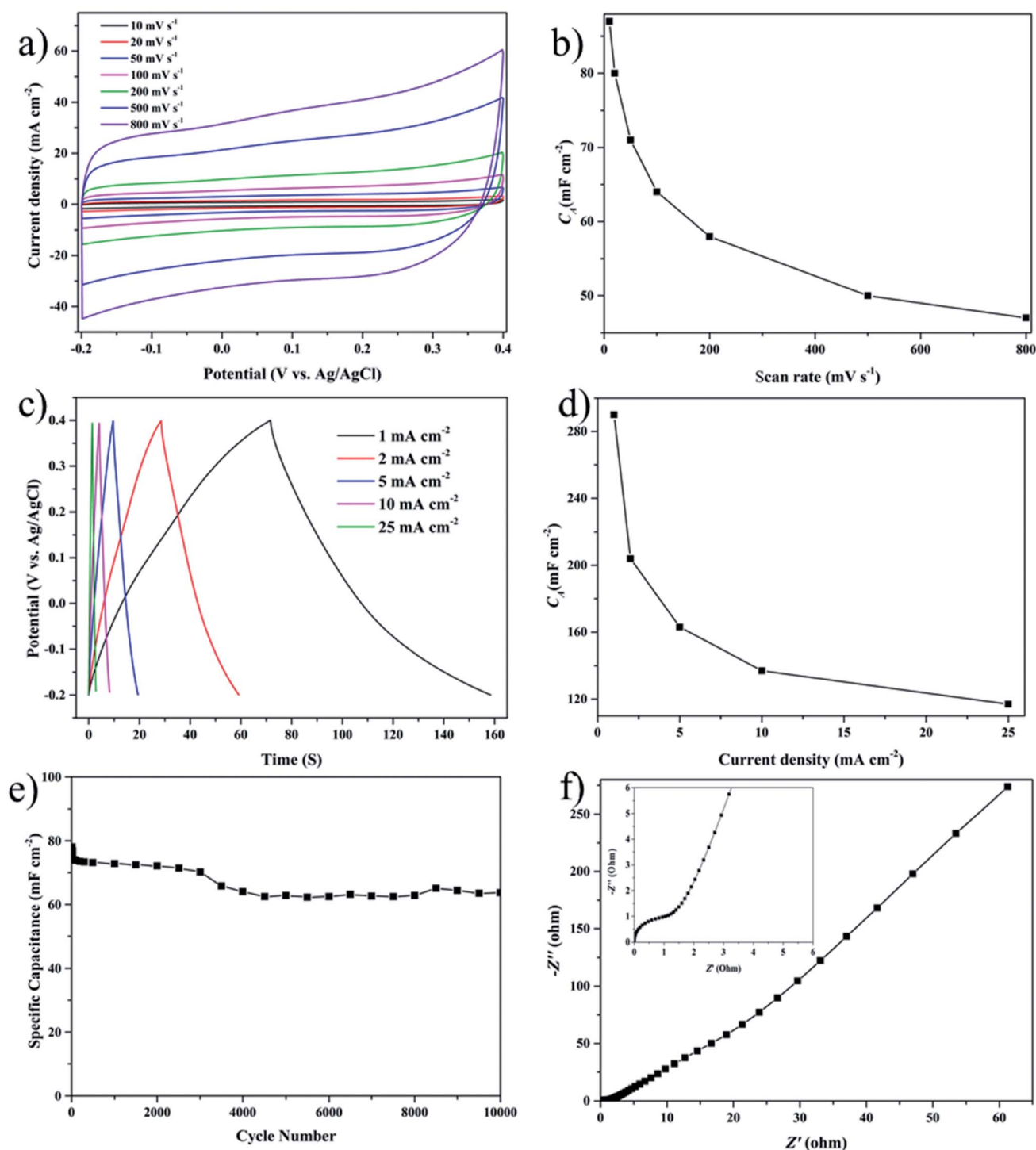


Fig. 4 Electrochemical energy storage performance of the rosette-like MoS<sub>2</sub> nanoflowers. (a) CV curves at different scan rates from 10 to 800 mV s<sup>-1</sup>; (b) corresponding specific capacitances at different scan rates; (c) galvanostatic charging–discharging (GCD) curves at current densities of 1, 2, 5, 10, and 25 mA cm<sup>-2</sup>; (d) the variation of capacitance at different current densities; (e) cycle stability analysis at a scan rate of 50 mV s<sup>-1</sup>; (f) Nyquist plots in the frequency range from 0.01 Hz to 100 kHz.

corresponding current densities are calculated and plotted in Fig. 4d. The  $C_A$  of the sample is 290, 204, 163, 137 and 117 mF cm<sup>-2</sup> at current densities of 1, 2, 5, 10 and 25 mA cm<sup>-2</sup>, respectively. The  $C_A$  decreases with increasing the current density, which is due to that the ion transport is difficulty in nanostructured materials with large surface area at high current

density. The  $C_A$  of the samples for 6 and 20 h are only 120 and 174 mF cm<sup>-2</sup> at current densities of 1 mA cm<sup>-2</sup> calculated from the curves in Fig. S6b,† respectively, which can also demonstrate the superiority of the as-prepared samples for 12 h. In addition, the specific capacitance achieves a maximum value of 137 mF cm<sup>-2</sup> at a low current density of 10 mA cm<sup>-2</sup>. This value



is appreciable when compared with previously reported supercapacitors based on MoS<sub>2</sub> materials (Table S2, ESI†). The high capacitance is attributed to the large surface area and the hierarchically layer structure of the sample, which provide shorter pathways for fast and efficient ion transport. Moreover, the specific capacitance kept on decreasing with the increase of current density, which is owing to the fact that almost all the available pores of the electrode are occupied by electrolyte ions at lower current densities.<sup>55</sup> To validate its practical application, the cyclic stability of samples is examined by CV measurement at 50 mV s<sup>-1</sup> in a potential window between -0.4 and 0.2 V. As shown in Fig. 4e, the specific capacitance of the sample continues to decrease between 3000 and 4000 cycles, and then stabilize constant. After 10 000 cycles, the specific capacitance remains a high capacitance retention of 81.6% after 10 000 cycles. The morphological properties of the samples after 3000 and 4000 cyclability are analyzed by SEM, and the images of the samples are displayed in Fig. S7.† From Fig. S7a,† the samples are still maintaining the original morphology of rosette-like nanoflowers after 3000 cycles, but the nanoflowers are covered by the substances after 4000 cycles (Fig. S7b†). So, the active site of the samples reduces after 3000 cycles, which results that the capacity continue to decrease between 3000 and 4000 cycles. After 3000 cycles, the pores are generated on the samples (Fig. S8†), which is beneficial to the transport of the electrons<sup>53</sup> and enhance the performance of the electrode material. Therefore, the capacity stabilizes after 4000 cycles. Fig. 4f shows the electrochemical impedance spectroscopy (EIS) curve of the MoS<sub>2</sub> nanoflowers from 0.01 Hz to 10 kHz (inset shows the equivalent circuit and the fitted equivalent circuit), which indicates an excellent EDLC behavior of the device and a small equivalent series resistance facilitating electrostatic adsorption of ions.<sup>56</sup> Obviously, such MoS<sub>2</sub> nanomaterial presents great potential in energy storage applications.

## 4. Conclusions

In summary, the rosette-like MoS<sub>2</sub> nanoflowers on Ti foil have been directly synthesized for the first time *via* a simple hydrothermal reaction. The as-prepared materials obtained by optimizing the synthesis time delivered excellent electrochemical performance towards the HER and supercapacitor. This is attributed to the unique 3D architectures and the enlarged interlayer spacing of the rosette-like MoS<sub>2</sub> nanoflowers, which is beneficial to the transport of ions and electrolyte. This work provided a new way to develop well-designed nanostructured materials for both efficient energy production and storage.

## Conflicts of interest

There are no conflicts to declare.

## Acknowledgements

This work was supported by the National Natural Science Foundation of China (21764007, 21662018), the Natural Science Foundation of the Jiangxi Province of China (20161BAB203082)

and Jiangxi Provincial Department of Education's Item of Science and Technology (GJJ160759, GJJ170653 and GJJ150760).

## References

- 1 G. Gershtinsky, E. Bar, L. Monconduit and D. Zitoun, Operando electron magnetic measurements of Li-ion batteries, *Energy Environ. Sci.*, 2014, 7, 2012–2016.
- 2 Q. Jiang, N. Kurra, M. Alhabeb, Y. Gogotsi and H. N. Alshareef, All pseudocapacitive MXene-RuO<sub>2</sub> asymmetric supercapacitor, *Adv. Energy Mater.*, 2018, 7, 1703043.
- 3 R. R. Salunkhe, Y. V. Kaneti and Y. Yamauchi, Metal-organic framework-derived nanoporous metal oxides toward supercapacitor applications: progress and prospects, *ACS Nano*, 2017, 11, 5293–5308.
- 4 Y. Y. Feng, H. J. Zhang, L. Fang, Y. P. Mu and Y. Wang, Uniquely Monodispersing NiFe Alloyed Nanoparticles in Three-Dimensional Strongly Linked Sandwiched Graphitized Carbon Sheets for High-Efficiency Oxygen Evolution Reaction, *ACS Catal.*, 2016, 6, 4477–4485.
- 5 Y. Jiao, Y. Zheng, K. Davey and S. Z. Qiao, Activity origin and catalyst design principles for electrocatalytic hydrogen evolution on heteroatom-doped graphene, *Nat. Energy*, 2016, 1, 16130.
- 6 D. Y. Wang, M. Gong, H. L. Chou, C. J. Pan, H. A. Chen, Y. P. Wu, M. C. Lin, M. Y. Guang, J. Yang, C. W. Chen, Y. L. Wang, B. J. Hwang, C. C. Chen and H. J. Dai, Highly Active and Stable Hybrid Catalyst of Cobalt-Doped FeS<sub>2</sub> Nanosheets-Carbo Nanotubes for Hydrogen Evolution Reaction, *J. Am. Chem. Soc.*, 2015, 137, 1587–1592.
- 7 Y. G. Wang, Y. F. Song and Y. Y. Xia, Electrochemical capacitors: mechanism, materials, systems, characterization and applications, *Chem. Soc. Rev.*, 2016, 45, 5925–5950.
- 8 F. C. Zheng, Y. Yang and Q. W. Chen, High lithium anodic performance of highly nitrogen-doped porous carbon prepared from a metal-organic framework, *Nat. Commun.*, 2014, 5, 5261.
- 9 Z. X. Wu, W. Lei, J. Wang, R. Liu, K. D. Xia, C. J. Xuan and D. L. Wang, Various structured molybdenum-based nanomaterials as advanced anode materials for lithium ion batteries, *ACS Appl. Mater. Interfaces*, 2017, 9, 12366–12372.
- 10 H. F. Lv, Z. Xi, Z. Z. Chen, S. J. Guo and Y. S. Yu, A New Core/Shell NiAu/Au Nanoparticle Catalyst with Pt-like Activity for Hydrogen Evolution Reaction, *J. Am. Chem. Soc.*, 2015, 137, 5859–5862.
- 11 Y. Y. Feng, H. J. Zhang, Y. X. Guan, Y. P. Mu and Y. Wang, Novel three-dimensional flower-like porous Al<sub>2</sub>O<sub>3</sub> nanosheets anchoring NiS<sub>2</sub> nanoparticles for high-efficiency hydrogen evolution, *J. Mater. Chem. A*, 2016, 4, 11507.
- 12 Y. Jiao, Y. Zheng, M. Jaronies and S. Z. Qiao, Design of electrocatalysts for oxygen- and hydrogen-involving energy conversion reactions, *Chem. Soc. Rev.*, 2015, 44, 2060–2086.
- 13 G. Li, X. L. Wang, J. Fu, J. D. Li, M. G. Park, Y. N. Zhang, G. Lui and Z. W. Chen, Pomegranate-Inspired Design of



- Highly Active and Durable Bifunctional Electrocatalysts for Rechargeable Metal-Air Batteries, *Angew. Chem., Int. Ed.*, 2016, **55**, 4977–4982.
- 14 D. Voiry, J. Yang and M. Chhowalla, Recent strategies for improving the catalytic activity of 2D TMD nanosheets toward the hydrogen evolution reaction, *Adv. Mater.*, 2016, **28**, 6197–6206.
  - 15 L. L. Feng, G. T. Yu, Y. Y. Wu, G. Li, Y. H. Sun, T. Asefa, W. Chen and X. X. Zou, High-Index Faceted  $\text{Ni}_3\text{S}_2$  Nanosheet Arrays as Highly Active and Ultrastable Electrocatalysts for Water Splitting, *J. Am. Chem. Soc.*, 2015, **137**, 14023–14026.
  - 16 E. J. Popczun, C. G. Read, C. W. Roske, N. S. Lewis and R. E. Schaak, Highly Active Electrocatalysis of the Hydrogen Evolution Reaction by Cobalt Phosphide Nanoparticles, *Angew. Chem., Int. Ed.*, 2014, **53**, 5427–5430.
  - 17 M. S. Faber and S. Jin, Earth-abundant inorganic electrocatalysts and their nanostructures for energy conversion applications, *Energy Environ. Sci.*, 2014, **7**, 3519–3542.
  - 18 M. S. Faber, R. Dziedzic, M. A. Lukowski, N. S. Kaiser, Q. Ding and S. Jin, High-Performance Electrocatalysis Using Metallic Cobalt Pyrite ( $\text{CoS}_2$ ) Micro- and Nanostructures, *J. Am. Chem. Soc.*, 2014, **136**, 10053–10061.
  - 19 W. F. Chen, K. Sasaki, C. Ma, A. I. Frenkel, N. Marinkovic, J. T. Muckerman, Y. M. Zhu and R. R. Adzic, Hydrogen-Evolution Catalysts Based on Non-Noble Metal Nickel–Molybdenum Nitride Nanosheets, *Angew. Chem., Int. Ed.*, 2012, **51**, 6131–6135.
  - 20 H. Vrubel and X. L. Hu, Molybdenum Boride and Carbide Catalyze Hydrogen Evolution in both Acidic and Basic Solutions, *Angew. Chem., Int. Ed.*, 2012, **51**, 12703–12706.
  - 21 E. J. Popczun, J. R. McKone, C. G. Read, A. J. Biacchi, A. M. Wiltrout, N. S. Lewis and R. E. Schaak, Nanostructured Nickel Phosphide as an Electrocatalyst for the Hydrogen Evolution Reaction, *J. Am. Chem. Soc.*, 2013, **135**, 9267–9270.
  - 22 J. F. Xie, H. Zhang, S. Li, R. X. Wang, X. Sun, M. Zhou, J. F. Zhou, X. W. Lou and Y. Xie, Defect-Rich  $\text{MoS}_2$  ultrathin nanosheets with additional active edge sites for enhanced electrocatalytic hydrogen evolution, *Adv. Mater.*, 2013, **25**, 5807–5813.
  - 23 Z. Y. Lu, H. C. Zhang, W. Zhu, X. Y. Yu, Y. Kuang, Z. Chang, X. D. Lei and X. M. Sun, In situ fabrication of porous  $\text{MoS}_2$  thin-films as high-performance catalysts for electrochemical hydrogen evolution, *Chem. Commun.*, 2013, **49**, 7516–7518.
  - 24 J. Kibsgaard, Z. B. Chen, B. N. Reinecke and T. F. Jaramillo, Engineering the surface structure of  $\text{MoS}_2$  to preferentially expose active edge sites for electrocatalysis, *Nat. Mater.*, 2012, **11**, 963–969.
  - 25 Z. B. Chen, D. Cummins, B. N. Reinecke, E. Clark, M. K. Sunkara and T. F. Jaramillo, Core-shell  $\text{MoO}_3$ - $\text{MoS}_2$  nanowires for hydrogen evolution: a functional design for electrocatalytic materials, *Nano Lett.*, 2011, **11**, 4168–4175.
  - 26 J. D. Benck, Z. B. Chen, L. Y. Kuritzky, A. J. Forman and T. F. Jaramillo, Amorphous molybdenum sulfide catalysts for electrochemical hydrogen production: Insights into the origin of their catalytic activity, *ACS Catal.*, 2012, **2**, 1916–1923.
  - 27 H. T. Wang, C. Tsai, D. S. Kong, K. Chan, F. Abild-Pedersen, J. K. Nørskov and Y. Cui, Transition-metal doped edge sites in vertically aligned  $\text{MoS}_2$  catalysts for enhanced hydrogen evolution, *Nano Res.*, 2015, **8**, 566–575.
  - 28 M. Khan, A. B. Yousaf, M. M. Chen, C. S. Wei, X. B. Wu, N. D. Huang, Z. M. Qi and L. B. Li, Molybdenum sulfide/graphene-carbon nanotube nanocomposite material for electrocatalytic applications in hydrogen evolution reactions, *Nano Res.*, 2016, **9**, 837–848.
  - 29 Z. X. Wu, J. Wang, R. Liu, K. D. Xia, C. J. Xuan, J. P. Guo, W. Lei and D. L. Wang, Facile preparation of carbon sphere supported molybdenum compounds (P, C and S) as hydrogen evolution electrocatalysts in acid and alkaline electrolytes, *Nano Energy*, 2017, **32**, 511–519.
  - 30 Z. X. Wu, J. Wang, K. D. Xia, W. Lei, X. Liu and D. L. Wang,  $\text{MoS}_2$ - $\text{MoP}$  heterostructured nanosheets on polymer-derived carbon as an electrocatalyst for hydrogen evolution reaction, *J. Mater. Chem. A*, 2018, **6**, 616–622.
  - 31 G. Wang, J. Y. Tao, Y. J. Zhang, S. P. Wang, X. J. Yan, C. C. Liu, F. Hu, Z. Y. He, Z. J. Zuo and X. W. Yang, Engineering Two-Dimensional Mass-Transport Channels of the  $\text{MoS}_2$  Nanocatalyst toward Improved Hydrogen Evolution Performance, *ACS Appl. Mater. Interfaces*, 2018, **10**, 25409–25414.
  - 32 J. Deng, H. B. Li, J. P. Xiao, Y. C. Tu, D. H. Deng, H. X. Yang, H. F. Tian, J. Q. Li, P. J. Ren and X. H. Bao, Triggering the electrocatalytic hydrogen evolution activity of the inert two-dimensional  $\text{MoS}_2$  surface via single-atom metal doping, *Energy Environ. Sci.*, 2015, **8**, 1594–1601.
  - 33 J. Kibsgaard, Z. B. Chen, B. N. Reinecke and T. F. Jaramillo, Engineering the surface structure of  $\text{MoS}_2$  to preferentially expose active edge sites for electrocatalysis, *Nat. Mater.*, 2012, **11**, 963–969.
  - 34 M. Saraf, K. Natarajan, A. K. Saini and S. M. Mobin, Small biomolecule sensors based on an innovative  $\text{MoS}_2$ -rGO heterostructure modified electrode platform: a binder-free approach, *Dalton Trans.*, 2017, **46**, 15848–15858.
  - 35 F. P. Wang, G. F. Li, J. F. Zheng, J. Ma, C. X. Yang and Q. Z. Wang, Hydrothermal synthesis of flower-like molybdenum disulfide microspheres and their application in electrochemical supercapacitors, *RSC Adv.*, 2018, **8**, 38945–38954.
  - 36 Z. Y. Ma, X. F. Zhou, W. Deng, D. Lei and Z. P. Liu, 3D Porous MXene ( $\text{Ti}_3\text{C}_2$ )/Reduced Graphene Oxide Hybrid Films for Advanced Lithium Storage, *ACS Appl. Mater. Interfaces*, 2018, **10**, 3634–3643.
  - 37 Y. Zhang, T. He, G. L. Liu, L. H. Zu and J. H. Yang, One-pot mass preparation of  $\text{MoS}_2/\text{C}$  aerogels for high-performance supercapacitors and lithium-ion batteries, *Nanoscale*, 2017, **9**, 10059–10066.
  - 38 G. L. Liu, Z. Y. Wang, L. H. Zu, Y. Zhang, Y. T. Feng, S. H. Yang, Y. Jia, S. Y. Wang, C. Zhang and J. H. Yang, Hydrogen evolution reactions boosted by bridge bonds





- between electrocatalysts and electrodes, *Nanoscale*, 2018, **10**, 4068–4076.
- 39 X. Q. Xie, T. Makaryan, M. Q. Zhao, K. L. Van Aken, Y. Gogotsi and G. X. Wang, MoS<sub>2</sub> Nanosheets Vertically Aligned on Carbon Paper: A Freestanding Electrode for Highly Reversible Sodium-Ion Batteries, *Adv. Energy Mater.*, 2016, **6**, 1502161.
  - 40 B. Ahmeda, D. H. Anjuma, Y. Gogotsi and H. N. Alshareef, Atomic layer deposition of SnO<sub>2</sub> on MXene for Li-ion battery anodes, *Nano Energy*, 2017, **34**, 249–256.
  - 41 K. Ma, H. Jiang, Y. J. Hu and C. Z. Li, 2D Nanospace Confined Synthesis of Pseudocapacitance-Dominated MoS<sub>2</sub>-in-Ti<sub>3</sub>C<sub>2</sub> Superstructure for Ultrafast, *Adv. Funct. Mater.*, 2018, **28**, 1804306.
  - 42 C. T. Zhao, C. Yu, M. D. Zhang, Q. Sun and S. F. Li, Enhanced sodium storage capability enabled by super wide-interlayer-spacing MoS<sub>2</sub> integrated on carbon fibers, *Nano Energy*, 2017, **41**, 66–74.
  - 43 Z. Pu, Q. Liu, A. M. Asiri, Y. Luo, X. Sun and Y. He, 3D microporous MoS<sub>2</sub> thin film: *in situ* hydrothermal preparation and application as a highly active hydrogen evolution electrocatalyst at all pH values, *Electrochim. Acta*, 2015, **168**, 133–138.
  - 44 Y. H. Chang, C. T. Lin, T. Y. Chen, C. L. Hsu, Y. H. Lee, W. Zhang, K. H. Wei and L. J. Li, Highly Efficient electrocatalytic hydrogen production by MoS<sub>x</sub> grown on graphene-protected 3D Ni foams, *Adv. Mater.*, 2013, **25**, 756–760.
  - 45 K. K. Liu, W. Zhang, Y. H. Lee, Y. C. Lin, M. T. Chang, C. Y. Su, H. Li, Y. Shi, H. Zhang, C. S. Lai and L. J. Li, Growth of large-area and highly crystalline MoS<sub>2</sub> thin layers on insulating substrates, *Nano Lett.*, 2012, **12**, 1538–1544.
  - 46 J. L. Yong, F. Chen, Y. Fang, J. L. Huo, Q. Yang, J. Z. Zhang, H. Bian and X. Hou, Bioinspired Design of Underwater Superaerophobic and Superaerophilic Surfaces by Femtosecond Laser Ablation for Anti- or Capturing Bubbles, *ACS Appl. Mater. Interfaces*, 2017, **9**, 39863–39871.
  - 47 C. Huang and Z. G. Guo, The wettability of gas bubbles: from macro behavior to nano structures to applications, *Nanoscale*, 2018, **10**, 19659–19672.
  - 48 J. L. Huang, D. M. Hou, Y. C. Zhou, W. J. Zhou, G. Q. Li, Z. H. Tang, L. G. Li and S. W. Chen, MoS<sub>2</sub> nanosheet-coated CoS<sub>2</sub> nanowire arrays on carbon cloth as three-dimensional electrodes for efficient electrocatalytic hydrogen evolution, *J. Mater. Chem. A*, 2015, **3**, 22886–22891.
  - 49 Y. G. Li, H. L. Wang, L. M. Xie, Y. Y. Liang, G. S. Hong and H. J. Dai, MoS<sub>2</sub> Nanoparticles Grown on Graphene: An Advanced Catalyst for the Hydrogen Evolution Reaction, *J. Am. Chem. Soc.*, 2011, **133**, 7296–7299.
  - 50 F. X. Ma, H. B. Wu, B. Y. Xia, C. Y. Xu and X. W. Lou, Hierarchical  $\beta$ -Mo<sub>2</sub>C Nanotubes Organized by Ultrathin Nanosheets as a Highly Efficient Electrocatalyst for Hydrogen Production, *Angew. Chem., Int. Ed.*, 2015, **54**, 15395–15399.
  - 51 M. Saraf, R. A. Dar, K. Natarajan, A. K. Srivastava and S. M. Mobin, A Binder-Free hybrid of CuO-Microspheres and rGO Nanosheets as an Alternative Material for Nest Generation Energy Storage Application, *ChemistrySelect*, 2016, **1**, 2826–2833.
  - 52 R. Zhou, C. J. Han and X. M. Wang, Hierarchical MoS<sub>2</sub>-coated three-dimensional graphene network for enhanced supercapacitor performances, *J. Power Sources*, 2017, **352**, 99–110.
  - 53 Y. Yang, H. L. Fei, G. D. Ruan, C. S. Xiang and M. T. James, Edge-oriented MoS<sub>2</sub> Nanoporous films as Flexible Electrodes for Hydrogen Evolution Reactions and Supercapacitor Devices, *Adv. Mater.*, 2014, **26**, 8163–8168.
  - 54 M. S. Raghua, K. Y. Kumar, S. Rao, T. Aravinda, S. C. Sharma and M. K. Prashanth, Simple fabrication of reduced graphene oxide-few layer MoS<sub>2</sub> nanocomposite for enhanced electrochemical performance in supercapacitors and water purification, *Phys. B*, 2018, **537**, 336–345.
  - 55 G. Zhang, H. J. Liu, J. H. Qu and J. H. Li, Two-dimensional layered MoS<sub>2</sub>: rational design, properties and electrochemical applications, *Energy Environ. Sci.*, 2016, **9**, 1190–1209.
  - 56 S. Mohit, N. Kaushik and M. M. Shaikh, Emerging Robust Heterostructure of MoS<sub>2</sub>-rGO for High-Performance Supercapacitors, *ACS Appl. Mater. Interfaces*, 2018, **10**, 16588–16595.

